



Exploring crystal phase and morphology in the TiO_2 supporting materials used for visible-light driven plasmonic photocatalyst

Chyan Kyung Song^{a,1}, Jayeon Baek^{a,1}, Tae Yong Kim^a, Sungju Yu^a, Jeong Woo Han^b, Jongheop Yi^{a,*}

^a World Class University Program of Chemical Convergence for Energy & Environment, School of Chemical and Biological Engineering, Institute of Chemical Processes, Seoul National University, Seoul 151-742, Republic of Korea

^b Department of Chemical Engineering, University of Seoul, Seoul 130-743, Republic of Korea



ARTICLE INFO

Article history:

Received 21 January 2016

Received in revised form 27 March 2016

Accepted 20 May 2016

Available online 24 May 2016

Keywords:

Photocatalysis

Localized surface plasmon resonances

Titanium dioxide

Time resolved photoluminescence

Crystal phase and morphology

ABSTRACT

The effects of crystal phase and morphology in TiO_2 on photocatalytic performance under visible light were experimentally and theoretically investigated. Results reveal that a rutile crystal phase with a three dimensional (3D) morphology was the most favorable supporting material for visible light driven photocatalyst among Au/TiO_2 s. The prolonged localized surface plasmon resonance (LSPR) lifetime and plasmonic coupling of Au induced by the 3D morphology of TiO_2 played a key role in enhancing photocatalytic activity. In addition, hot electrons generated on Au by LSPR are preferentially transferred to rutile TiO_2 due to the overlapping of density of states (DOS) of Au in the conduction band of rutile TiO_2 but obstruction of the reverse directional transfer of electrons to Au by large band bending. Our results provide a strategy for designing suitable plasmonic photocatalysts based on the crystal phase and morphology of TiO_2 for solar light-driven photocatalysis applications.

© 2016 Elsevier B.V. All rights reserved.

1. Introduction

In recent researches directed at photocatalysis, plasmonic noble metal supported on a semiconductor is one of the promising topics, since this material can be activated under visible light [1–16]. The main focuses in this area have been on applying various semiconductor materials [17,18], regulating morphologies [19,20], and designing efficient multi-heterojunction materials [21–23]. For the rationally and entirely considered design of plasmonic photocatalyst material, microscopic aspect of metal–semiconductor interface and optical aspect coming from morphology need to be considered at the same time.

TiO_2 is one of the most widely investigated semiconductor material in photocatalysis because of low cost, non-toxic and high chemical stability [24]. It is still a converversal issue that which phase of TiO_2 is appropriate for plasmonic photocatalysis. It is generally known that, anatase TiO_2 is more effective than rutile TiO_2 in conventional photocatalysis in the UV light region by virtue

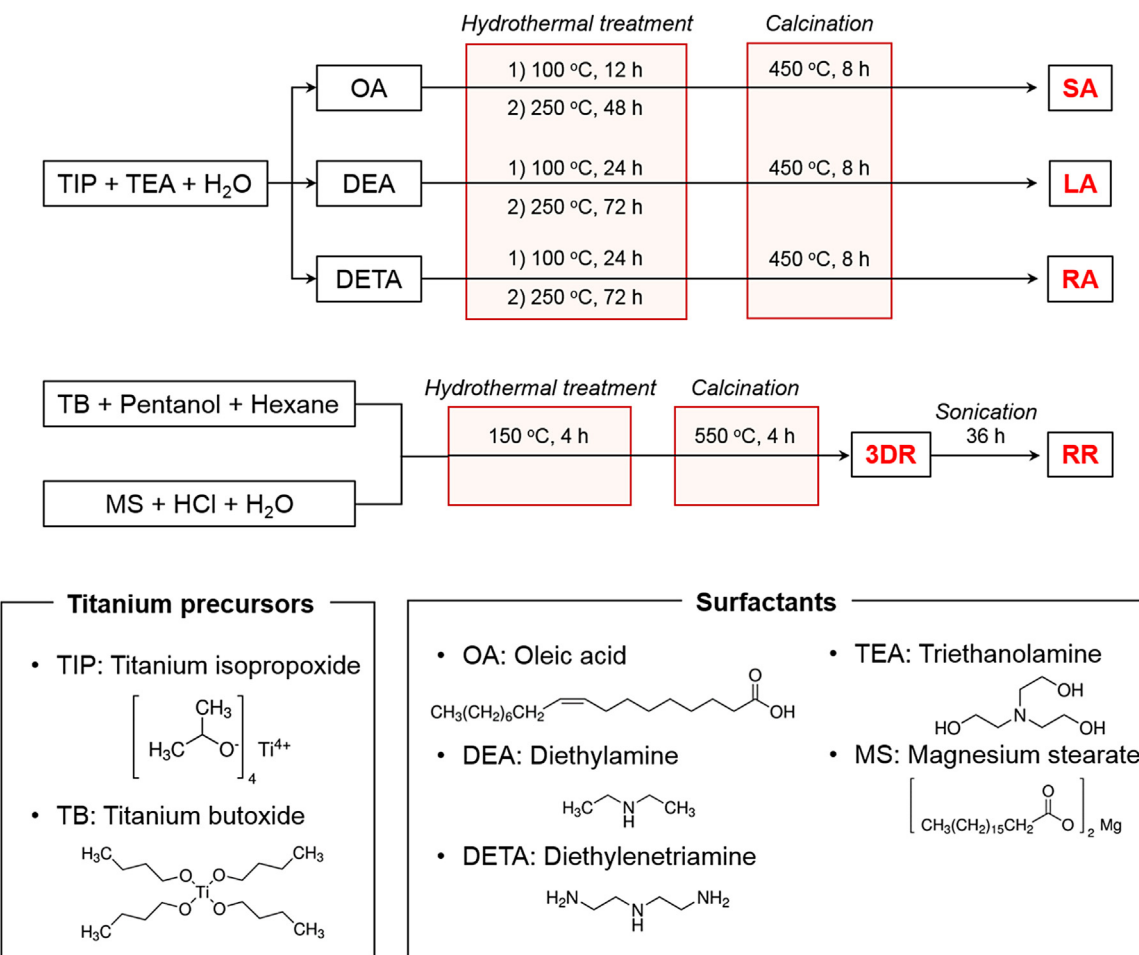
of the facile electron–hole separation and higher exciton mobility [25–27]. There are a few reports indicating that the photocatalytic activity of gold-loaded rutile TiO_2 ($\text{Au}/\text{rutile TiO}_2$) is better than $\text{Au}/\text{anatase TiO}_2$ under conditions of visible light irradiation. Naya et al. [28] and Kimuuura et al. [29] reported that elongation of the LSPR lifetime in the Au/rutile system favors the interfacial electron transfer from Au to rutile TiO_2 , but there is no quantitative evidence for why $\text{Au}/\text{rutile TiO}_2$ is superior than $\text{Au}/\text{anatase TiO}_2$. Importantly, these reports support our argument that those criteria should be reconsidered in the aspect of microscopic and optical for plasmonic photocatalysis.

In the microscopic aspect of metal–semiconductor interface, semiconductor material with high electric permittivity can contribute to large amount of charge separation between metal and semiconductor, when proper metal–semiconductor bonding and Fermi energy (E_F) level difference exist. TiO_2 is one of the strong candidates among semiconductor materials, especially rutile TiO_2 polymorphs, exhibits relatively large permittivity ($\epsilon(\text{rutile TiO}_2)=114$ and $\epsilon(\text{anatase TiO}_2)=48$). E_F and band level of TiO_2 are well suited with E_F of plasmonic noble metal for the formation of Schottky barrier, which acts as obstacle for electron transfer from TiO_2 to Au but enables electron transfer from Au to TiO_2 by local surface plasmon resonance (LSPR).

* Corresponding author.

E-mail address: jyi@snu.ac.kr (J. Yi).

¹ These authors contributed equally to this work.



Scheme 1. Schematic diagram for the preparing methods of a series of TiO_2 s.

Furthermore, in the optical aspect, 3D morphology of semiconductor as a supporting material decorated with plamonic metal nanoparticles can modulate the direction of light irradiation on the coupled nanoparticles. In the closely spaced Au nanoparticle arrays, it is observed that transverse or longitudinal mode of plasmonic coupling happens, respectively depending on irradiated light direction, which affects the LSPR wavelength and extinction intensity [30]. In the light of this feature, it is expected that radially symmetric 3D mesoporous structure material can get irradiated light with the same direction regardless of orientation, although randomly oriented 0D sphere, 1D rod, or 2D sheet structure material cannot have any priority in direction of light irradiation.

In the present study, complementary approaches of experimental and computational analyses are attempted to explore and disclose that how the crystal phase and morphology of TiO_2 influence plasmonic photocatalytic activity. The TiO_2 samples used in this work were small anatase TiO_2 spheres (SA), large anatase TiO_2 spheres (LA), anatase TiO_2 rods (RA), rutile TiO_2 rods (RR), and 3D hierarchical rutile TiO_2 (3DR). Based on these materials, 2 wt.% Au/ TiO_2 heterostructures were synthesized by a deposition-precipitation method. *p*-nitrosodimethylaniline (RNO) was representatively used for the measurement of plasmonic photocatalytic activity of a series of Au/ TiO_2 s. RNO is a dye which can only be degraded by hydroxyl radical [31], which indicates that self photodegradation or photodegradation by direct charge transfer between Au/ TiO_2 and adsorbed RNO is negligible. Hydroxyl radical has been known to be the main component for the degra-

dation of organic compounds. Dark field microscope (DFM) and a finite-difference time-domain (FDTD) simulation was conducted to identify the morphological aspect, and time-resolved photoluminescence (TR-PL) and density functional theory (DFT) calculations to the microscopic aspect.

Results presented here highlight LSPR lifetime of hot electrons, plasmonic coupling effect in the morphological aspect, interfacial electron transfer rate between Au and TiO₂, Au density of states (DOS), and band bending in the crystal phase aspect, respectively. Our results provide insight into the factors important to design heterostructure using TiO₂ as supporting material for photocatalyst under visible light (>455 nm).

2. Experimental methods and computational details

2.1. Preparation of Au/TiO₂s heterostructures

TiO₂s were synthesized to have different morphology and phase. Scheme 1 shows the schematic diagram for the fabrication process of a series of TiO₂s. Three types of anatase TiO₂ particles were prepared, as described in our previous report [32]. Small anatase TiO₂ spheres (SA) were synthesized by the gel-sol method. A 0.4 mol triethanolamine ($\geq 98\%$, Aldrich) and a 0.2 mol titanium(IV) isopropoxide ($\geq 99.0\%$, Samchun) were mixed for 30 min, and deionized water (D.I. water) was then added to a total volume of 400 ml, followed by mixing for 30 min until the color of the solution changed to yellow. A 30 ml aliquot of this solution was added

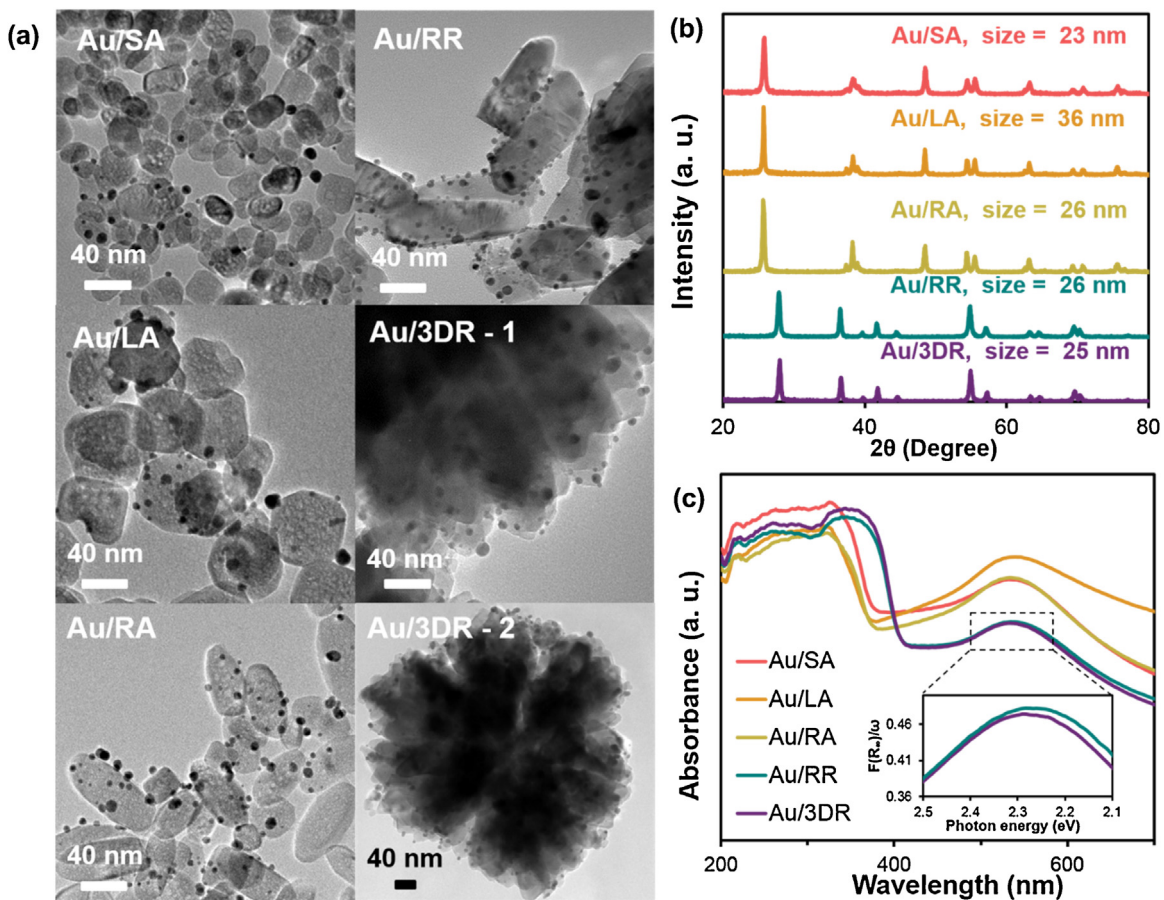


Fig. 1. (a) HR-TEM images; Au/3DR-1: High-magnified image and Au/3DR-2: low magnified image (b) XRD spectra with calculated TiO₂ crystallite sizes, and (c) UV-vis DRS spectra of a series of 2 wt.% Au/TiO₂ heterostructures. In the absorption part of LSPR, units of axis were converged for calculations of LSPR linewidth and indicated inset (SA: small anatase TiO₂ spheres, BA: large anatase TiO₂ spheres, RA: anatase TiO₂ rods, RR: rutile TiO₂ rods, and 3DR: 3D hierarchical rutile TiO₂).

to 30 ml of 0.02 M oleic acid (Samchun), which was used as a surfactant. The mixtures were transferred to a Teflon-lined autoclave and heated at 100 °C for 12 h and then at 250 °C for 48 h. The light red colored precipitate obtained was washed three times with D.I. water and isolated by centrifugation. The product was dried at 70 °C for 12 h and calcined at 450 °C for 8 h. LA and RA were synthesized by varying the type of surfactant and hydrothermal treatment time. Diethylamine was used as a surfactant in LA and diethylenetriamine in RA. The hydrothermal treatment process was 100 °C for 24 h and then 250 °C for 72 h both in case of large anatase TiO₂ spheres (LA) and anatase TiO₂ rods (RA). 3D hierarchical rutile TiO₂ (3DR) was synthesized by a micro-emulsion method [33]. Briefly, titanium *n*-butoxide (TiBu, 97%, Aldrich) was used as the TiO₂ precursor and magnesium stearate (Riedel-de Haën) was used as the surfactant. Aqueous and oil crystal phases were separately prepared and then mixed. In the case of the aqueous crystal phase, 30 ml of 2.6 M hydrochloric acid (35~37%, Samchun) was mixed with 0.7686 g magnesium stearate. In the case of the oil crystal phase, 4.5 ml *n*-amyl alcohol (99%, Samchun) was added to 30 ml of cyclohexane (≥99%, Aldrich) as a cosolvent and 4.0 ml TiBu was mixed with that solution. The oil phase was first stirred for 20 min before mixing and then stirred for 30 min after mixing. The total solution was transferred to a Teflon-lined autoclave and subjected to a heat treatment at 150 °C for 4 h. The resulting precipitate was centrifuged with D.I. water and ethanol (1:1, v/v) for several times, dried at 70 °C for 12 h and then calcined at 550 °C for 4 h. Rutile TiO₂ rods (RR) was produced from 3DR by ultrasonication treatment for 36 h at the

concentration of 1 g TiO₂/30 ml D.I. water. The final product was then collected by centrifugation and dried at 70 °C for 12 h.

All Au/TiO₂ heterostructures are prepared with 2 wt.% of Au loading. The 2 wt.% Au/TiO₂ heterostructures were synthesized by deposition-precipitation method. A 0.3 g sample of the prepared TiO₂ sample was added to a 100 ml of HAuCl₄·4H₂O (≥99.9%, Aldrich) solution, which contained the same equivalent of 0.006 g of Au. The pH was then adjusted to ~7 with a 0.05 M NaOH (≥98.0%, Samchun) solution prior to stirring for 12 h in dark condition. Since then, 50 ml of NaBH₄ (99%, Aldrich) solution containing NaBH₄ 10 times more than of the amount of Au was dropwisely injected to the solution and stirred for 1 h. The product was centrifuged and washed with D.I. water for several times, and finally dried at 70 °C for 12 h.

2.2. Photocatalytic activity test

RNO was selected as a representative organic compound for photodegradation because RNO is only degraded by hydroxyl radicals. Hydroxyl radicals are known to be the main component in the degradation of organic matter. 0.1 g of Au/TiO₂ photocatalyst was added to 100 ml of 3 ppm RNO solution and dispersed by stirring for 5 h in the dark. The photodegradation was then conducted under visible light, using a 300 W Xe lamp with a 455 nm cut-on filter. The decrease in the concentration of RNO was measured by UV-vis spectroscopy (V670-Jasco) in the range of 200–800 nm at an interval of 1 h after filtering the catalyst. Absorbance at 439 nm

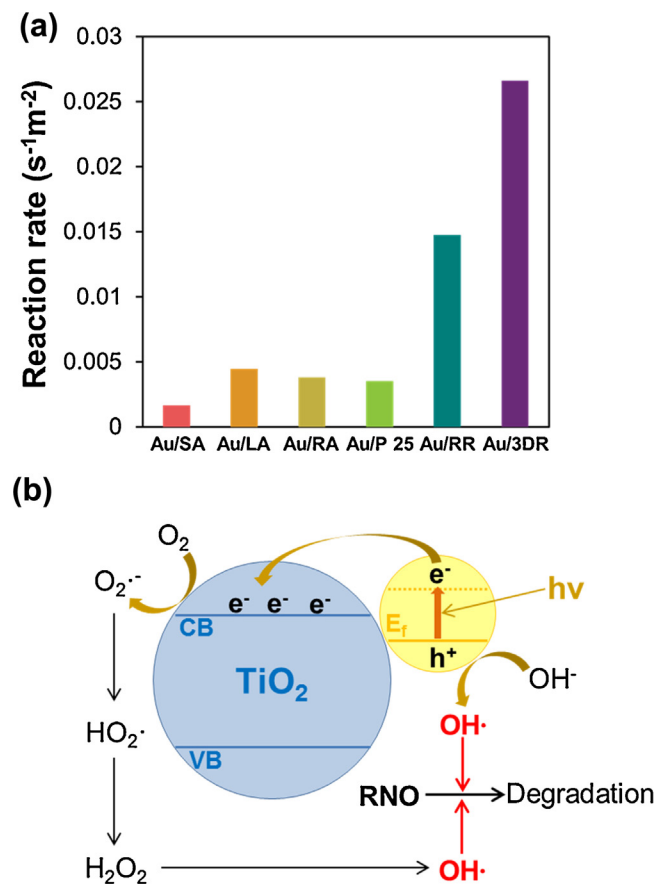


Fig. 2. (a) Photocatalytic degradation of RNO in the presence of a series of 2 wt.% Au/TiO₂ heterostructures under visible light (>455 nm filter). (b) Hydroxyl radical formation path in Au/TiO₂ under visible light. RNO is degraded by hydroxyl radical.

wavelength was identified as the highest and used for the analysis of first-order reaction based photodegradation rate constants.

2.3. Characterization of materials

The shapes of the TiO₂ and gold nanoparticle size distribution were observed by high-resolution transmission electron microscopy (HR-TEM, JEM 3010-JEOL, 300 kV) equipped with energy-dispersive X-ray spectroscopy (EDS, Oxford) and field-emission scanning electron microscopy (FE-SEM, SUPRA 55VP, Carl Zeiss). The elemental chemical status was observed by X-ray photoelectron spectroscopy (XPS, AXIS-HSi, KRATOS). The final content of Au in a series of Au/TiO₂s was determined by inductive coupled plasma atomic emission spectrometry (ICP-AES, OPTIMA 4300DV). The crystal phases of Au/TiO₂ were defined by X-ray diffractometry (XRD, D/max-2500/PC-Rigaku) with Cu K α radiation ($\lambda = 1.5406 \text{ \AA}$) as an incident beam at operating mode of 50 kV and 100 mAN₂ adsorption-desorption analysis was conducted at 77 K using ASAP 2010 (Micromeritics). The surface area of Au/TiO₂ was calculated by the BET method in the range of $P/P_0 = 0.1\text{--}0.2$. Pore size distribution and pore volume were obtained from the absorption branches using BJH methods. Analytical high-angle annular dark-field scanning transmission electron microscope (HAADF-STEM, Tecnai F20-FEI, 200 kV) equipped with EDS (Tecnai 136-5-EDAX) was used for 2D atomic mapping of Ti, Au, and O. FT-IR spectrophotometer (Nicolet 6700) was used to identify the amount of surface hydroxyl group in a series of Au/TiO₂s. The dark-field micro-spectroscopic system is a combination of a commercial Axio Observer Z1 inverted microscope (Carl Zeiss, Germany), a true-color digital camera, a 1024 pixel 256 pixel cooled spectrograph CCD

camera (Andor Technology PLC, UK) and a home-built micro-fluidic chamber. The spectrophotometer (Monora320i, Dongwoo Optron Co., Korea) had dual-turret holding gratings of 1200 grooves/mm and 300 grooves/mm. A programmable shutter was mounted internal to an adjustable entrance slit, the width of which could be opened to retain only a single nanoparticle in the region of interest.

2.4. Photoluminescence test

All photoluminescence (PL) data were obtained at a concentration of 0.01 g of sample/10 ml of solution, which is the same conditions as were used in the photodegradation test. PerkinElmer LS55 spectrophotometer (PerkinElmer Ltd., Beaconsfield, UK) equipped with a Xe lamp was used for the measurement of steady-state PL of a series of TiO₂ and Au/TiO₂ heterostructures. Time-resolved PL was measured by using 1 μM of rhodamine B dye (RhB, Aldrich, for fluorescence) solution according to time correlated single photon counting methods by using FluoTime 200 instrument (Picoquant GmbH). A 500 nm pulsed diode laser (LDH-P-C-500, Picoquant GmbH, pulse energy = 10 pJ; FWHM < 54 ps) with the repetition rate of 80 MHz was used as an excitation source. The measured results from the PicoHarp 300 were analyzed by the FluoFit software.

2.5. Computational details

OptiFDTD version 12.0 was used to perform the FDTD simulations. Two 10 nm size Au NPs were located inside a $0.6 \mu\text{m} \times 0.3 \mu\text{m} \times 0.3 \mu\text{m}$ domain. In the case of two coupled Au NPs, the gap was designated to 2 nm, whereas

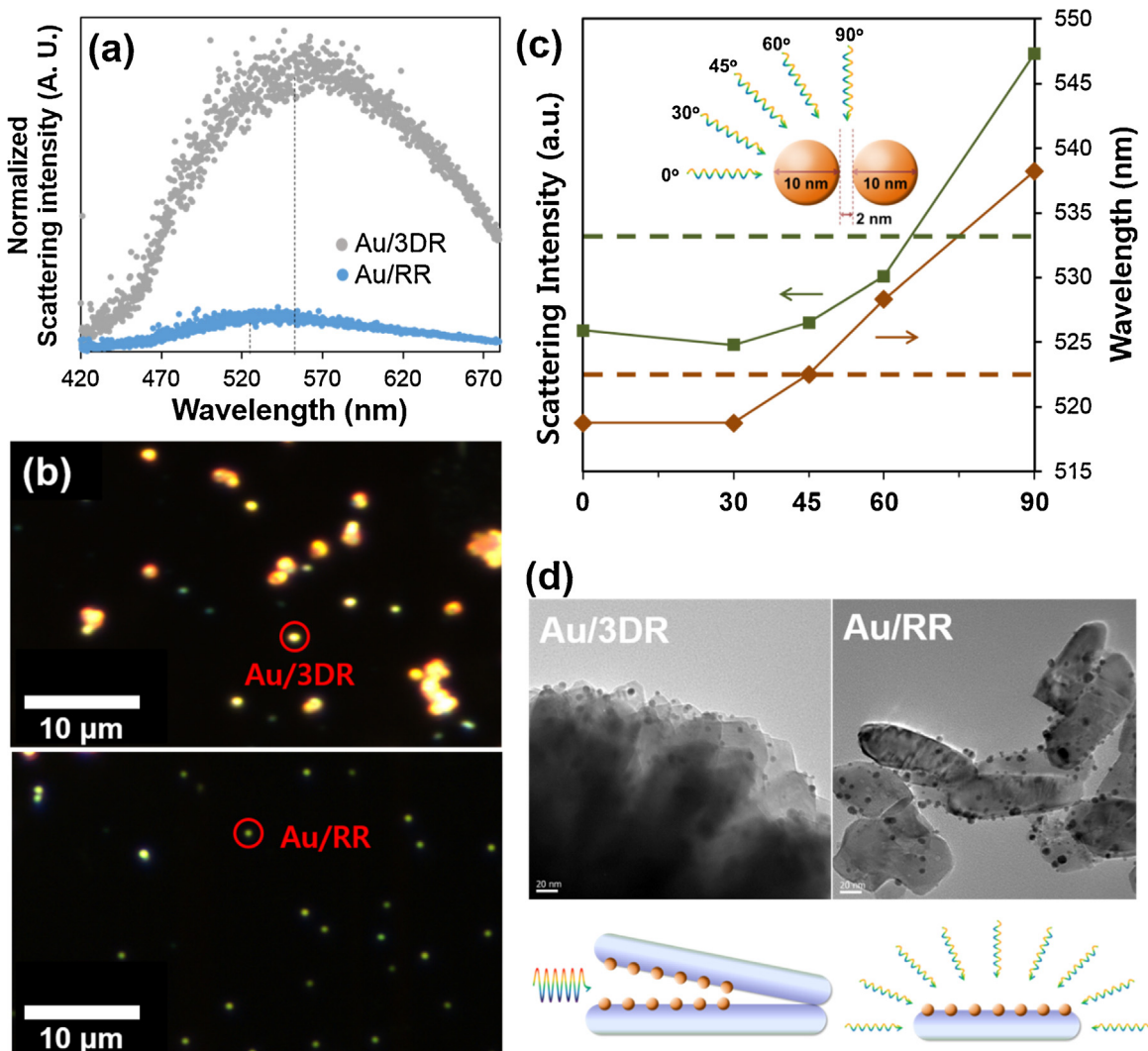


Fig. 3. (a) and (b) Below are dark field images of Au/3DR and Au/RR. Typical particles were selected and are indicated by red circles. Dark-field scattering spectra were obtained from corresponding particles and normalized with BET surface area (Table S2). (c) FDTD simulations were performed according to inset scheme of coupled Au NPs with light irradiation in different directions. Derived wavelength and intensity were presented, and the values of original 10 nm Au NP were indicated by dotted lines. (d) TEM images of Au/3DR and Au/RR are listed above. Simplified schemes of Au/3DR and Au/RR including light irradiation are contained below. (For interpretation of the references to colour in this figure legend, the reader is referred to the web version of this article.)

100 nm for two independent Au NPs. Mesh parameters were $0.001 \mu\text{m} \times 0.001 \mu\text{m} \times 0.001 \mu\text{m}$, and time step size was 1.668×10^{-18} with 12000 time steps. A 550 nm wavelength rectangular Gaussian modulated continuous wave was directed along the z-axis, and a discrete Fourier transform between $0.4 \mu\text{m} \sim 0.9 \mu\text{m}$ was performed to derive power spectrum of Au NPs. Periodic boundary condition (PBC) was applied to x and y-direction, and anisotropic perfectly matched layer (APML) to z-direction to perform the FDTD simulation.

Periodic density functional theory (DFT) calculations were carried out using the Vienna ab initio simulation package (VASP) [34]. We employed the generalized gradient approximation (GGA) parameterized by Perdew-Burke-Ernzerhof (PBE) exchange-correlation functional [35]. Ionic cores were described by the projector augmented wave (PAW) method [36]. The wave functions were constructed from the expansion of planewaves with an energy cutoff of 400 eV. A $1 \times 1 \times 1$ Monkhorst-Pack k-point mesh was used to sample the Brillouin zone. All calculations were converged until the forces on all atoms were less than $0.03 \text{ eV}/\text{\AA}$. The electronic optimization steps were converged self-consistently to $< 2 \times 10^{-5} \text{ eV}$. For the calculation of bulk optimization, the cut-off energy was

increased to 520 eV and a $6 \times 6 \times 4$ k-point mesh was used. The surface was constructed by cleaving the optimized bulk structure along the (101) surface of anatase TiO_2 and the (110) surface of rutile TiO_2 , which are the most abundant surface in the practical case. To prevent in-physical electronic interactions, 20 Å of the vacuum region between the slabs was added. Both (101) anatase TiO_2 and (110) rutile TiO_2 surfaces largely consisted of 3 layers and the top 2 layers were allowed to relax while the residual bottom layer was fixed. In the DOS calculations, $2 \times 2 \times 1$ Gamma-Centered k-point mesh was used. DFT+U within Dudarev's approach was used with $U_{\text{eff}} = 3.5$ [37,38] to account for the on-site Coulomb interaction in the localized Ti 3d orbital.

3. Results and discussion

3.1. Physicochemical and optical property of 2 wt.% Au/ TiO_2

The physicochemical properties of prepared samples were proved by FE-SEM, HR-TEM, EDS, ICP-AES, N_2 adsorption-desorption curve, and XRD measurement (Fig. S1-S3 and Table S1, S2). The coterminous sized Au nanoparticles (NPs) were evenly dis-

tributed on TiO_2 to exclude metal size effects in localized surface plasmon resonance (LSPR) (Fig. 1a and Figs. S4, S5). The Au NP size distribution is listed in Fig. S4 where the overall average size of Au is in the range of 6.1~6.5 nm. The own characteristic crystal phases of TiO_2 s were determined by XRD measurement which were not changed by Au loading (Fig. 1b). Importantly, the crystallite size of anatase TiO_2 rods (RA) and rutile TiO_2 rods (RR), as calculated using the Scherrer equation, is the same at 26 nm, which permits the precise analysis of the crystal phase effect. The crystallite size of rutile TiO_2 in RR or 3DR was also observed by HR-TEM with FFT analysis (Fig. S6). The rutile TiO_2 crystallite with 30 nm by 17 nm size was identified. The light absorption property of a series of TiO_2 and Au/ TiO_2 heterostructures was measured by UV-vis DRS (Fig. 1c and Fig. S7). The peaks of TiO_2 (~400 nm) in Au loaded RR and 3D hierarchical rutile TiO_2 (3DR) were red shifted to a larger extent than the corresponding peaks in Au loaded small anatase TiO_2 spheres (SA), large anatase TiO_2 spheres (LA), and RA due to the lower bandgap of pristine rutile TiO_2 than anatase TiO_2 . The peaks in all samples were slightly extended into the visible light region because of the formation of surface states in which Au and TiO_2 are in contact [39]. The characteristics of the LSPR lifetime was identified from homogeneous LSPR linewidth in the region of visible light (Γ_{hom}), which can be calculated from the intrinsic Fano analysis of $F(R_\infty)/\omega$ obtained from absorbance values of Au/ TiO_2 s [40–42]. The LSPR lifetime is related to the LSPR dephasing time T_2 , and T_2 is a function of Γ_{hom} by the equation, $T_2 = 2\hbar/\Gamma_{\text{hom}}$. From the LSPR parts of Au/RR and Au/3DR spectra, Γ_{hom} was calculated to be 0.434 eV in Au/RR, and 0.422 eV in Au/3DR (see inset of Fig. 1c), which means that the LSPR lifetime of Au/3DR is longer. The same result was observed between Au/SA and Au/RA. Thus, it can be concluded that the lifetime of hot electrons generated by LSPR phenomenon are affected by the morphology of TiO_2 and with the order of sphere < rod < 3D hierarchical structure.

3.2. Photocatalytic degradation of RNO

For a comparison of photocatalytic performance under visible light (>455 nm for exclusion of possibility of TiO_2 excitation, as 3.0 eV bandgap of rutile TiO_2 can absorb light up to 413 nm), RNO, which is known to be only degraded by hydroxyl radical, was used as a model organic compound (Fig. 2a). Hydroxyl radicals can be produced from both electron sites in TiO_2 CB and hole sites in Au NPs (Fig. 2b) [43]. The photocatalytic activities of Au/ TiO_2 heterostructures were in the order of Au/SA < Au/P 25 < Au/RA < Au/LA < Au/RR < Au/3DR. Generally, Au supported on rutile TiO_2 s showed a much better performance than Au supported on anatase TiO_2 s. Regarding the effect of structure, the photodegradation rate of Au supported on the 3D hierarchical structure was faster than that for the rod form (Au/RR < Au/3DR) and the Au supported on rod was faster than that for the sphere (Au/SA < Au/RA), which corresponds to the LSPR lifetime (Fig. 1c). For the determination of relationship between TiO_2 surface and photocatalytic activity, the difference of surface hydroxyl group generated by a series of TiO_2 s were comparatively analyzed. In Fig. S8, the FT-IR spectra of a series of Au/ TiO_2 s show broad band in the region of 3550–3100 cm^{-1} , which stands for Ti-OH stretching modes [44–48]. The absorption of Ti-OH stretching mode of a series of Au/ TiO_2 s were in the order of Au/RR ≈ Au/3DR < Au/RA ≈ Au/LA < Au/SA, which shows similar trend with BET surface areas of a series of Au/ TiO_2 s (Table S2). As the surface hydroxyl group of TiO_2 can act as a charge trap site for the photocatalysis and enhances charge separation [49], the amount of the surface hydroxyl group is known to be the determining factor for photocatalytic activity when bare TiO_2 is used as a photocatalyst. Thus, the photocatalytic activity tendency is expected to be Au/RR ≈ Au/3DR < Au/RA ≈ Au/LA < Au/SA in the

general semiconductor photocatalytic system. However, the actual plasmonic photocatalytic activity under visible light was the order of Au/SA < Au/P 25 < Au/RA < Au/LA < Au/RR < Au/3DR, which shows the reverse trend. Since charge separation occurs between Au and TiO_2 CB in the plasmonic photocatalytic system, plasmonic coupling of Au NPs and interaction between Au and TiO_2 can also be the major factors for improving photocatalytic activity.

3.3. Effect of morphology in rutile phase TiO_2

The enhanced plasmonic coupling in Au/3DR was observed by DFM. Since samples were prepared by drop casting on glass, there are a few aggregated parts. Thus, single particle which shows the same absorption spectrum with UV-vis DRS were selected for the measurement of scattering spectra (Fig. 3a and b). After white light irradiation on a single particle, a substantial red shift in the LSPR peak and amplified plasmonic coupling in Au/3DR were observed [50]. To verify the advantage of a 3D structure, plasmonic coupling of two Au NPs depending on the irradiated light angle was calculated by means of the FDTD simulation (Fig. 3c). When the tilted angle is lower than 45°, the transverse mode becomes more dominant than the longitudinal mode and a blue shift with decreased intensity of electromagnetic (EM) field in the LSPR peak occurs. When the tilted angle is higher than 45°, the longitudinal mode is formed and the reverse phenomenon happens. It should be noted that transverse mode coupling severely obstructs the EM field amplification from the longitudinal mode coupling. Even when the tilted angle is 60° where the longitudinal mode is dominant, the power intensity is smaller than that from independent Au NP. However, when it reaches 90°, a dramatic increases in intensity of the EM field as well as red shift occurs. Rods from Au/RR are randomly oriented in the photocatalytic system and plasmonic coupling effects in all angles are negatively averaged. On the other hand, rods in the Au/3DR are oriented in an orderly manner and most of the Au NP array can be irradiated by light in the vertical direction. This confined structure effect facilitate the strongly amplified longitudinal plasmonic coupling, which leads the LSPR peak of Au/3DR becomes red-shift with high intensity (Fig. 3d).

3.4. Interfacial charge transfer rate comparison in 2 wt.% Au/ TiO_2 heterostructures

TR-PL was conducted to quantitatively examine the hot electron transfer rate from Au NPs to TiO_2 CB using 500 nm excitation laser (Fig. 4), which is correlated with the generation of hydroxyl radicals. Prior to the TR-PL measurement, characteristic PL emissions of a Rhodamine B (RhB) dye solution and an aqueous solution of TiO_2 were observed by steady-state photoluminescence (SS-PL) spectra (Fig. S9). The maximum SS-PL of RhB was 580 nm with a 500 nm wavelength excitation and all of the TiO_2 and Au/ TiO_2 samples exhibited a 580 nm wavelength emission as well. For the TR-PL analysis, all of the TiO_2 and Au/ TiO_2 samples were dispersed in 1 μM RhB aqueous solution. Measured spectra were fitted to the sum of three exponential decay functions expressed as:

$$I(t) = \sum_{i=1}^n A_i e^{\frac{t}{\tau_i}} \quad (1)$$

The emission of RhB was expressed by a one exponential function and that of TiO_2 also by a one exponential function. In the case of TiO_2 and Au/ TiO_2 in the RhB solution, the derived parameters are listed in Table S3. As shown in the proposed scheme in Table S4, the governing equation can be expressed by two exponential decay functions [51,52]. We calculated the relative electron transfer rate constants from Au to TiO_2 ($k_{\text{R} \rightarrow \text{A} \rightarrow \text{T}}$) (for detail electron transfer paths, governing equations, and analytical solutions, see Table S4).

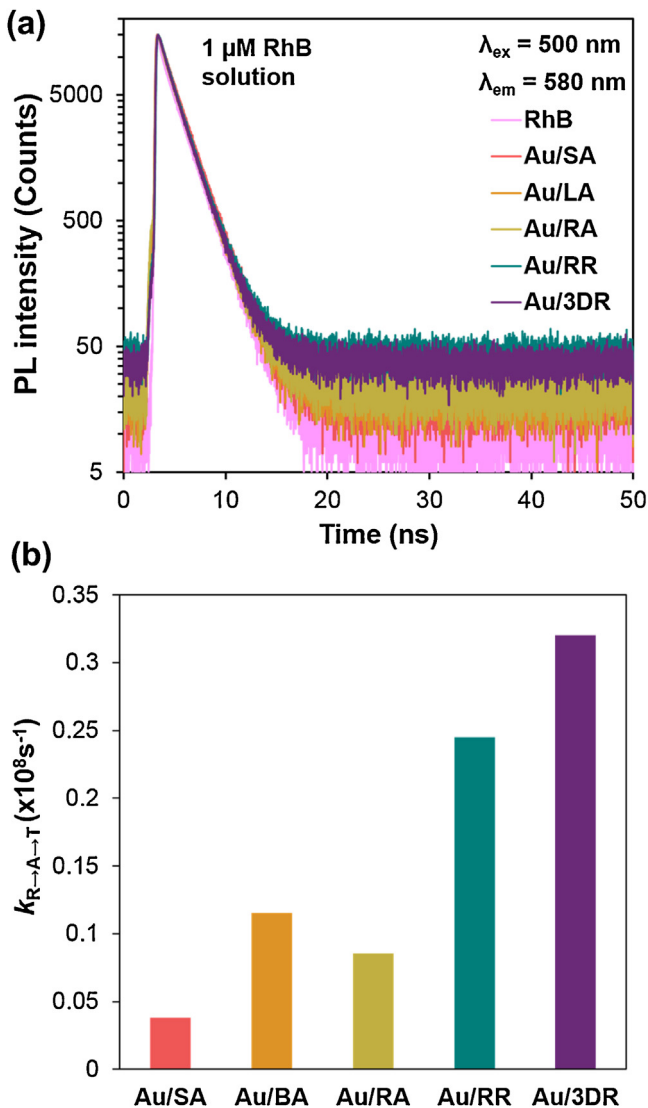
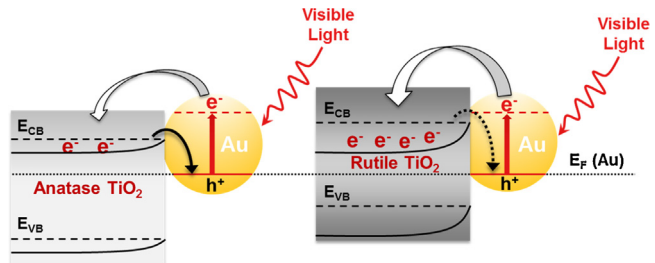


Fig. 4. (a) TR-PL spectra of Au/TiO₂ in RhB solution. (b) $k_{\text{R} \rightarrow \text{A} \rightarrow \text{T}}$ values of a series of Au/TiO₂ heterostructures. The values were derived from parameters obtained from TR-PL spectra.

The $k_{\text{R} \rightarrow \text{A} \rightarrow \text{T}}$ values of a series of Au/TiO₂ heterostructures are presented in Fig. 4b and other electron transfer rate constants are listed in Table S5. It should be noted that the tendency of $k_{\text{R} \rightarrow \text{A} \rightarrow \text{T}}$ corresponds to the photocatalytic activity in Fig. 2. This indicates that a faster electron-hole formation in Au which is in junction with TiO₂ improved photocatalytic activity. It is noticeable that $k_{\text{R} \rightarrow \text{A} \rightarrow \text{T}}$ of Au/RR is about 2.9 times higher than that of Au/RA in spite of their similar structure, crystallite size, and aspect ratio. Thus, the main reason for this difference can be attributed to a crystal phase effect.

The detail crystal phase effect was explored using DFT calculations. The binding energy (ΔE) of Au and DOS in the two crystal phases of Au/TiO₂s were calculated. Especially, we chose (101) plane for anatase and (110) plane for rutile which is the most stable plane for each crystal phase, respectively [53,54]. The findings indicate that the binding energies of Au in almost all of the possible binding sites in (110) rutile TiO₂ are much stronger than those in (101) anatase TiO₂ (Table 1). For a more precise examination, the DOS of TiO₂ and Au/TiO₂ were calculated and compared. When Au is bonded with rutile TiO₂, a $\sim 0.294 \text{ eV}$ band shift was observed, while that for anatase TiO₂ was $\sim 0.002 \text{ eV}$ which is negligible. This difference can be related to the extent of the contribution of Au DOS



Scheme 2. Schematic energy band diagram of two types of Au/TiO₂, showing the proposed electron transfer processes under visible light.

to each of the TiO₂ crystal phase. In the case of Au/anatase TiO₂, Au DOS mainly exists below the Fermi level and is totally included in the anatase TiO₂ VB. On the other hand, in the case of Au/rutile TiO₂, Au DOS partially exists above the Fermi level and is, in part, included to the rutile TiO₂ CB. This suggests that totally different hot electron transfer paths can exist for the two TiO₂ crystal phases. At the Au and anatase TiO₂ interface, hot electrons generated by LSPR can only transfer to anatase TiO₂ by electron tunneling effect since there are no Au states in anatase TiO₂ CB. However, at the interface between Au and rutile TiO₂ CB, a direct, hot electron transfer is possible in the presence of Au DOS in rutile TiO₂ CB. Therefore, the amount of transferred electrons between Au and rutile TiO₂ should be much more than that for anatase TiO₂ by efficient electron transfer aided by the stronger and closer binding of Au with rutile TiO₂.

3.5. Discussion of different energy band diagram between Au/anatase TiO₂ and Au/rutile TiO₂

Here, the Schottky barrier (φ_{SB}) is not the determining factor for $k_{\text{R} \rightarrow \text{A} \rightarrow \text{T}}$. As hot electrons generated by LSPR have a sufficient energy of 2.48 eV which is much higher than the E_F of Au to overpass the barrier. However, considering the reverse directional electron transfer path (TiO₂ \rightarrow Au), the Schottky barrier (φ_{SB}) or the potential of band bending (V_{BB}) needs to be considered. For example, according to the RNO photodegradation data (Fig. 2a) and the TR-PL spectra (Fig. 4), Au/LA showed a better photocatalytic activity and a higher $k_{\text{R} \rightarrow \text{A} \rightarrow \text{T}}$ than Au/SA in spite of their same crystal phase. These results can be attributed to the excessively small size of SA that precludes it from forming a depletion layer (D) or a space charge region [55]. The calculation indicates that the V_{BB} of TiO₂ is only $\sim 0.004 \text{ V}$ when the particle radius equals to the Debye length (L_D , 3.8–12 nm, with $\varepsilon_r \approx 100$ and $N_d \approx 10^{24}–10^{25} \text{ m}^{-3}$) as following equation [56]:

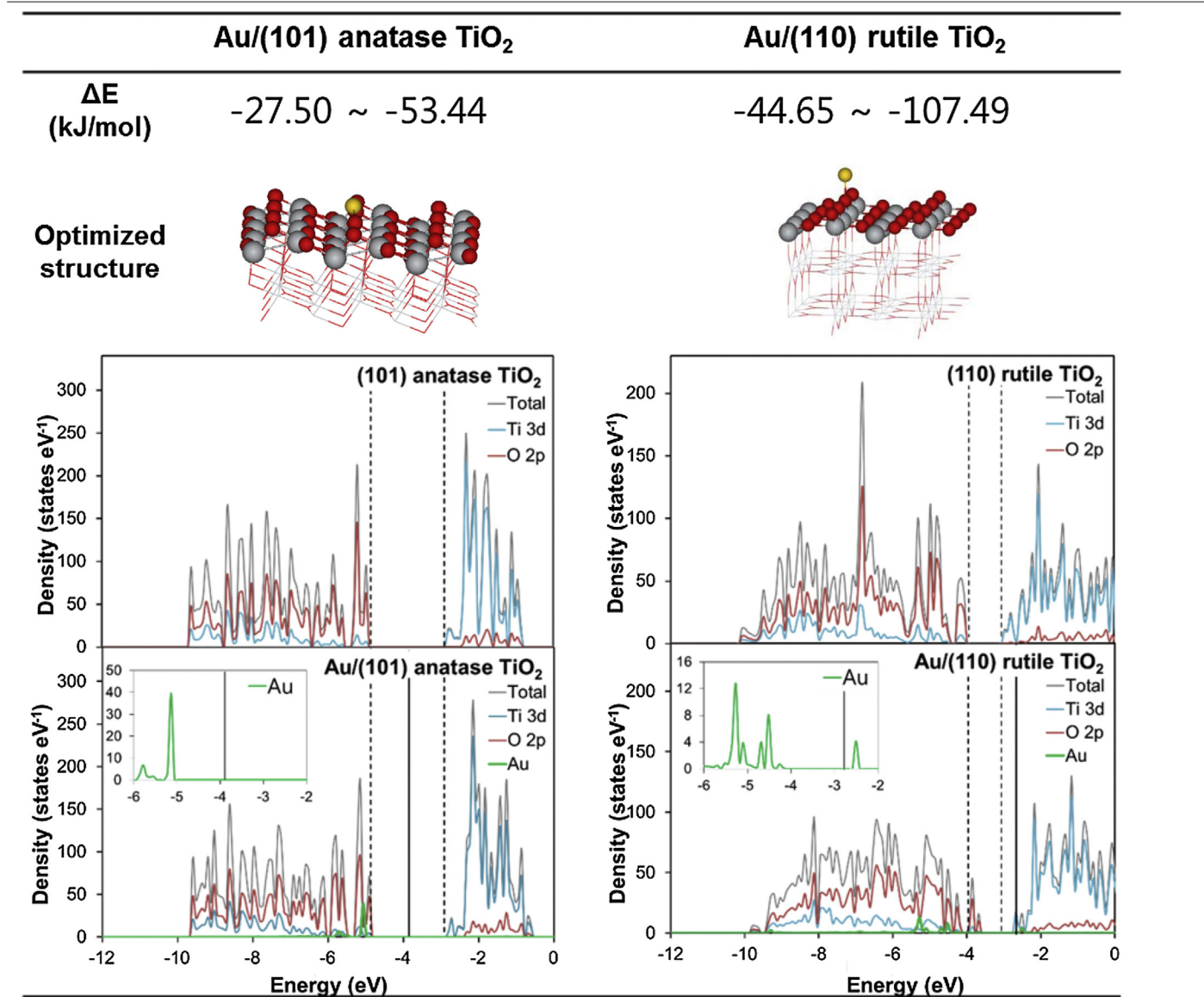
$$V_{\text{BB}} = \frac{eN_d D^2}{2\varepsilon_r \varepsilon_0} \quad (2)$$

A Au/SA heterostructure would cause an incomplete depletion layer and a low V_{BB} , which enables the easy overpass of electrons from TiO₂ CB to Au, resulting in a fast electron-hole recombination on Au. Likewise, this phenomenon is identically applied to the crystal phase effect. As discussed above, significant band shift ($\sim 0.294 \text{ eV}$) in Au/rutile TiO₂ induces a larger V_{BB} which results in slower electron-hole recombination.

A proposed electron transfer process for the two types of Au/TiO₂ under visible light is presented in Scheme 2 based on above results. Stronger and closer binding is formed between Au and rutile TiO₂, which enables electrons to flow from Au to rutile TiO₂ more easily than in case of anatase TiO₂. It was once considered that the CB minimum in anatase TiO₂ is $\sim 0.2 \text{ eV}$ higher than rutile TiO₂. However, an opposite view has arisen to be fact in the recent studies, which supports the conclusion that the CB minimum in rutile TiO₂ is $\sim 0.2 \text{ eV}$ higher than anatase TiO₂ [57,58]. Hence, both φ_{SB}

Table 1

DFT calculation results for Au/anatase TiO₂ and Au/rutile TiO₂. Binding energies of every possible sites, the most stable structure, and DOS spectra coming from those structures are listed. In the DOS spectra, dashed lines indicate CB minimum and VB maximum of TiO₂, and continuous lines indicate E_F of Au/TiO₂. E_F of TiO₂ matches with VB maximum line.



and V_{BB} would be expected to be higher in the Au/rutile TiO₂ system. Furthermore, due to the higher band shift in Au/rutile TiO₂ observed in DFT calculations, V_{BB} becomes higher which delays electron-hole recombination. Therefore, it can be concluded that more electrons are transferred from Au to rutile TiO₂ and less electrons are transferred from rutile TiO₂ to Au than in case of anatase TiO₂.

4. Conclusions

In this study, Au supported on 3D hierarchical rutile TiO₂ was verified as an optimized plasmonic photocatalyst under conditions of visible light by considering crystal phase and morphology, which are considered to be two basic factors. We were able to observe a prolonged LSPR lifetime and enhanced Au plasmonic coupling in 3D morphology by a confined structure effect. In the light of photocatalytic activity, which is deeply related to the rate of generation of hydroxyl radicals, the hot electron transfer rate from Au to TiO₂ ($k_{R \rightarrow A \rightarrow T}$) appears to be the main determinant. When $k_{R \rightarrow A \rightarrow T}$ was

compared under conditions of the same morphology and a different crystal phase of Au/TiO₂, Au/rutile TiO₂ showed a 2.9 times higher value than Au/anatase TiO₂. The findings revealed that due to the stronger bond between Au and rutile TiO₂ and the overlapping of Au DOS in the rutile TiO₂ CB, Au/rutile TiO₂ is more advantageous in both hot electron transfer and the quantity of electrons. Furthermore, the reverse transfer path is obstructed in Au/rutile TiO₂, due to the larger band bending induced by thermodynamic energy level of rutile TiO₂ CB, which delays the recombination between electrons and holes in Au.

Acknowledgement

This research was supported by the Supercomputing Center/Korea Institute of Science and Technology Information with supercomputing resources including technical support (KSC-2014-C2-055). This work was also supported by the National Research Foundation of Korea (NRF) grant funded by the Korea government (MEST) (No. 2013R1A2A2A01067164) and Global Frontier

R&D Program on Center for Multiscale Energy System funded by the National Research Foundation under the Ministry of Science, ICT & Future, Korea (NRF-2011-0031571).

Appendix A. Supplementary data

Supplementary data associated with this article can be found, in the online version, at <http://dx.doi.org/10.1016/j.apcatb.2016.05.047>.

References

- [1] T. Hirakawa, P.V. Kamat, *J. Am. Chem. Soc.* 127 (2005) 3928–3934.
- [2] J. Yu, G. Dai, B. Huang, *J. Phys. Chem. C* 113 (2009) 16394–16401.
- [3] Z. Liu, W. Hou, P. Pavaskar, M. Ayko, *Nano Lett.* 11 (2011) 1111–1116.
- [4] N. Chandrasekaran, P.V. Kamat, *J. Phys. Chem. B* 104 (2000) 10851–10857.
- [5] Y. Tian, T. Tatsuma, *J. Am. Chem. Soc.* 127 (2005) 7632–7637.
- [6] C.G. Silva, R. Juárez, T. Marino, R. Molinari, H. García, *J. Am. Chem. Soc.* 133 (2011) 595–602.
- [7] G. Zhou, X. Xu, T. Ding, B. Feng, Z. Bao, J. Hu, *ACS Appl. Mater. Interfaces* 7 (2015) 26819–26827.
- [8] F.-X. Xiao, Z. Zeng, S.-H. Hsu, S.-F. Hung, H.M. Chen, B. Liu, *ACS Appl. Mater. Interfaces* 7 (2015) 28105–28109.
- [9] C. Yu, W. Zhou, L. Zhu, G. Li, K. Yang, R. Jin, *Appl. Catal. B* 184 (2016) 1–11.
- [10] C. Yu, G. Li, S. Kumar, H. Kawasaki, R. Jin, *J. Phys. Chem. Lett.* 4 (2013) 2847–2852.
- [11] S. Bouhadoun, C. Guillard, F. Dapozze, S. Singh, D. Amans, J. Bouclé, N. Herlin-Boime, *Appl. Catal. B* 174–175 (2015) 367–375.
- [12] M. Tahir, B. Tahir, N.A.S. Amin, *Appl. Surf. Sci.* 356 (2015) 1289–1299.
- [13] L.G. Devi, R. Kavitha, *Appl. Surf. Sci.* 360 (2016) 601–622.
- [14] X. Wang, R. Yu, K. Wang, G. Yang, H. Yu, *Chin. J. Catal.* 36 (2015) 2211–2218.
- [15] J. Jiang, J. Yu, S. Cao, *J. Colloid Interface Sci.* 461 (2016) 56–63.
- [16] S. Das, S. Sinha, M. Suar, S.-I. Yun, A. Mishra, S.K. Tripathy, *J. Photochem. Photobiol. B* 142 (2015) 68–76.
- [17] D. Jiang, W. Wang, S. Sun, L. Zhang, Y. Zheng, *ACS Catal.* 5 (2015) 613–621.
- [18] F. Meng, S.K. Cushing, J. Li, S. Hao, N. Wu, *ACS Catal.* 5 (2015) 1949–1955.
- [19] L. Wu, F. Li, Y. Xu, J.W. Zhang, D. Zhang, G. Li, H. Li, *Appl. Catal. B* 164 (2015) 217–224.
- [20] C. Chen, M. Chen, C.K. Chen, P.C. Wu, P. Chen, M. Basu, S. Hu, D.P. Tsai, R. Liu, *Chem. Commun.* 51 (2015) 549–552.
- [21] J. Li, Y. Xie, Y. Zhong, Y. Hu, *J. Mater. Chem. A* 3 (2015) 5474–5481.
- [22] L. Sinatra, A.P. LaGrow, W. Peng, A.R. Kirmani, A. Amassian, H. Idriss, O.M. Bakr, *J. Catal.* 322 (2015) 109–117.
- [23] S. Zhang, J. Li, X. Wang, Y. Huang, M. Zeng, J. Xu, *J. Mater. Chem. A* 3 (2015) 10119–10126.
- [24] Y. Ma, X. Wang, Y. Jia, X. Chen, H. Han, C. Li, *Chem. Rev.* 114 (2014) 9987–10043.
- [25] T. Luttrell, S. Halpegamage, J. Tao, A. Kramer, E. Sutter, M. Batzill, *Sci. Rep.* 4 (2014) 4043–4050.
- [26] H. Tang, K. Prasad, R. Sanjinés, P.E. Schmid, F. Lévy, *J. Appl. Phys.* 75 (1994) 2042–2047.
- [27] E. Yagi, R.R. Hasiguti, M. Aono, *Phys. Rev. B* 54 (1996) 7945–7956.
- [28] S. Naya, T. Niwa, T. Kume, H. Tada, *Angew. Chem. Int. Ed.* 53 (2014) 7305–7309.
- [29] K. Kimuura, S. Naya, Y. Jin-nouchi, H. Tada, *J. Phys. Chem. C* 116 (2012) 7111–7117.
- [30] S.A. Maier, P.G. Kik, H.A. Atwater, *Appl. Phys. Lett.* 81 (2002) 1714–1716.
- [31] I. Kraljić, C.N. Trumbore, *J. Am. Chem. Soc.* 87 (1965) 2547–2550.
- [32] H.J. Yun, H. Lee, J.B. Joo, W. Kim, J. Yi, *J. Phys. Chem. C* 113 (2009) 3050–3055.
- [33] J. Baek, S. Park, C.K. Song, T.Y. Kim, J. Yi, *Chem. Commun.* 51 (2015) 15019–15022.
- [34] G. Kresse, J. Furthmüller, *Phys. Rev. B* 54 (1996) 11169–11186.
- [35] J.P. Perdew, K. Burke, M. Ernzerhof, *Phys. Rev. Lett.* 77 (1996) 3865–3868.
- [36] P.E. Blöchl, *Phys. Rev. B* 50 (1994) 17953–17979.
- [37] S.L. Dudarev, G.A. Botton, S.Y. Savrasov, C.J. Humphreys, A.P. Sutton, *Phys. Rev. B* 57 (1998) 1505–1509.
- [38] U. Aschauer, A. Selloni, *Phys. Chem. Chem. Phys.* 14 (2012) 16595–16602.
- [39] Z.W. She, M. Low, S. Zhang, Z. Liu, A. Mlayah, M. Han, *Adv. Mater.* 24 (2012) 2310–2314.
- [40] T. Klar, M. Perner, S. Grosse, G.V. Plessen, W. Spirk, J. Feldmann, *Phys. Rev. Lett.* 80 (1998) 4249–4252.
- [41] M. Hu, J. Chen, M. Marquez, Y. Xia, G.V. Hartlind, *J. Phys. Chem. C* 111 (2007) 12558–12565.
- [42] S. Naya, A. Inoue, H. Tada, *ChemPhysChem* 12 (2011) 2719–2723.
- [43] A. Houas, H. Lachheb, M. Ksibi, E. Elaloui, C. Guillard, J. Herrmann, *Appl. Catal. B* 31 (2001) 145–157.
- [44] Y.F. Chen, C.H. Lee, M.Y. Yeng, H.T. Chiu, *J. Cryst. Growth* 247 (2003) 363–370.
- [45] S. Watson, D. Beydoun, J. Scott, R. Amal, *J. Nanopart. Res.* 6 (2004) 193–207.
- [46] T. Bezrodnaa, G. Puchkovska, V. Shymanovska, J. Baranb, H. Ratajczak, *J. Mol. Struct.* 700 (2004) 175–181.
- [47] R.J. Tayade, R.K. Surolia, R.G. Kulkarni, R.V. Jasra, *Sci. Technol. Adv. Mater.* 8 (2007) 455–462.
- [48] J.-H. Kim, H.-I. Lee, *Korean J. Chem. Eng.* 21 (2004) 116–122.
- [49] G. Liu, X. Wang, Z. Chen, H.-M. Cheng, G.Q. Lu, *J. Colloid Interface Sci.* 329 (2009) 331–338.
- [50] H. Wang, T. You, W. Shi, J. Li, L. Guo, *J. Phys. Chem. C* 116 (2012) 6490–6494.
- [51] S. Yu, Y.H. Kim, H.Y.S.Y. Lee, H.D. Song, J. Yi, *Angew. Chem. Int. Ed.* 54 (2014) 11203–11207.
- [52] S. Yu, S.Y. Lee, J. Yeo, J.W. Han, J. Yi, *J. Phys. Chem. C* 118 (2014) 29583–29590.
- [53] M. Ramamoorthy, D. Vanderbilt, R.D. King-Smith, *Phys. Rev. B* 49 (1994) 16721–16727.
- [54] H. Zhang, J.F. Banfield, *J. Mater. Chem.* 8 (1998) 2073–2076.
- [55] A. Hagfeldt, M. Grätzel, *Chem. Rev.* 95 (1995) 49–68.
- [56] Z. Zhang, J.T. Yates, *Chem. Rev.* 112 (2012) 5520–5551.
- [57] D.O. Scanlon, C.W. Dunnill, J. Buckeridge, S.A. Shevlin, A.J. Logsdail, S.M. Woodley, C.R.A. Catlow, M.J. Powell, R.G. Palgrave, I.P. Parkin, G.W. Watson, T.W. Keal, P. Sherwood, A. Walsh, A.A. Sokol, *Nat. Mater.* 5 (2013) 798–801.
- [58] G. Xiong, R. Shao, T.C. Droubay, A.G. Joly, K.M. Beck, S.A. Chambers, W.P. Hess, *Adv. Funct. Mater.* 17 (2007) 2133–2138.